Flow Measurement and Instrumentation 99 (2024) 102674

Contents lists available at ScienceDirect

Flow Measurement and Instrumentation

journal homepage: www.elsevier.com/locate/flowmeasinst

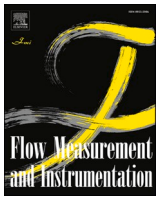

A numerical analysis of pressure characteristics in the deflector jet pilot stage valve with an innovative deflector deflection

Jinghui Peng [a], Bijan Krishna Saha [b,*], Md Shah Najmus Shakib [b], Songjing Li [a], Jahidul Islam Jihan [c]

[a] Department of Fluid Control and Automation, Harbin Institute of Technology, Harbin, 150001, China
[b] Department of Mathematics, Faculty of Science and Engineering, University of Barishal, Barishal, 8254, Bangladesh
[c] Department of Mechanical Engineering, Hajee Mohammad Danesh Science and Technology University, Dinajpur, 5200, Bangladesh

ARTICLE INFO

Keywords:
Electro-hydraulic servo-valve (EHSV)
Deflector jet servo-valve (DJSV)
Pressure and flow distribution
Cavitation
Computational fluid dynamics (CFD)

ABSTRACT

Electric-hydraulic servo-valves are extensively used in the aerospace, mechanical, and aerodynamics industries to control missile wings or airplanes precisely. Aiming to reduce undesired flow phenomena inside the deflector jet pilot valve, innovative deflections of deflector are proposed in this paper. A numerical analysis is performed using STAR CCM + to investigate the pressure and flow characteristics inside the pilot stage of deflector jet servo-valve. For observing the pressure, cavitation and flow characteristics, the Eulerian multi-phase model, VOF phase interaction, and realizable $k-\varepsilon$ model for the turbulent flow are used during numerical simulations. The supply and outlet pressure are kept at 24 MPa and 1 MPa, respectively. To verify the calculated numerical results for turbulent flows, the velocity distribution to the V-groove exit of the deflector jet pilot stage is calculated and discussed with the theoretical results. The numerically calculated results show good agreement with published analytical results. The result shows that by the innovative rotation of the deflector both in clockwise and anti-clockwise directions, significant pressure in the receivers is obtained than traditionally moving deflector to the left and right for the same supply pressure. Moreover, when the deflector is positioned clockwise or anti-clockwise by 5°, less cavitation is observed than in the traditional model. The key finding of this paper shows that innovative structural optimization of the amplifier disk and deflector is of utmost importance.

1. Introduction

The electrohydraulic servo-valve is a component of the power amplifier [1]. Using electricity, an electrohydraulic servo-valve controls the flow of hydraulic fluid to an actuator. Controlling massive hydraulic cylinders with an extremely small electrical signal is a common application of servo-valves. In addition to delivering accurate regulation of force, pressure, position, and velocity, servo-valves also exhibit beneficial post-movement damping properties. Servo-valves are crucial in the aerospace industry for thrust vector control of rockets and for ensuring the precise movement of aircraft control surfaces. To improve the accuracy of production processes, servo-valves are used in CNC machines, industrial robots, and injection molding machines. Moreover, servo-valves are used in mobile equipment to regulate hydraulic cylinder movements in agricultural and construction machines. Improved servo-valves can reduce costs and make these devices more accessible. Additionally, research helps integrate servo-valves with emerging technologies, enhancing automation and smart systems. So, ongoing research in servo-valves is essential for the advancement of many industries, making machinery more precise, efficient, and adaptable to modern technology. In the 1950s, MIT's faculty trained industrial engineers how to construct hydraulic control valves, and that knowledge is documented in the landmark book published by Blackburn, Shearer, and Reethof [1,2]. When considering single or two-stage servo-valve design approximately sixty-seven years ago, during the mid-1950s, a number of the foundational concepts were already in place. Following its introduction in the aerospace sector during the 1960s, the two-stage mechanical feedback servo-valve subsequently acquired prominence in high-performance manufacturing. Due in large part to the incorporation of electrical spool position feedback and integrated electronics, the single-stage valve with a corresponding solenoid or linear force motor direct spool valve became a more cost-effective option for a variety of industrial applications during the 1970s and 1980s [2,3]. The use of electrohydraulic servo-valves is rapidly expanding in the field of

* Corresponding author.
E-mail address: bksaha@bu.ac.bd (B.K. Saha).

https://doi.org/10.1016/j.flowmeasinst.2024.102674
Received 15 April 2024; Received in revised form 12 August 2024; Accepted 16 August 2024
Available online 22 August 2024

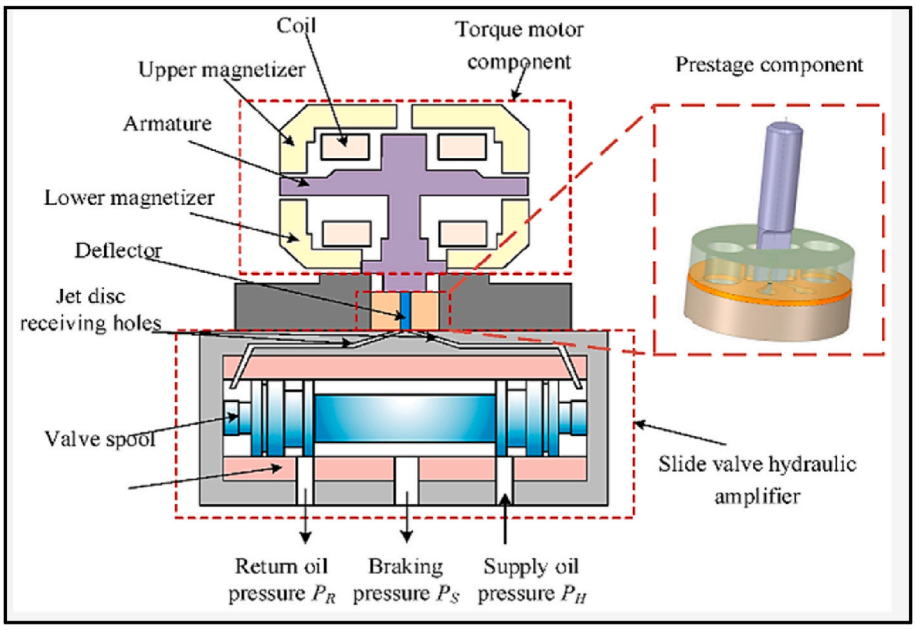

Fig. 1. Schematic diagram of the DJSV [26].

intelligent hydraulic control systems. Servo-valve innovation and development are moving into a potential new area of study. The crucial factor in preserving the overall functionality of an electrohydraulic servo-valve is the pilot stage, which functions as an electro-mechanical converter. Pilot stage components include a hydraulic amplifier and an electromagnetic torque motor [4]. The inception of servo-valves for fluid control and gearbox transpired prior to World War II in response to the requirements of the weapons industry. There are nowadays, deflector jet servo-valves (DJSVs), nozzle flapper servo-valves (NFSVs), jet pipe servo-valves (JPSVs), and direct drive servo valves (DDSVs) among the electro-hydraulic servo-valve family's several decades of expansion [5,6]. Hydraulic servo control systems significantly rely on servo-valves in high-tech industries such as aerospace, nuclear power, automobile engineering, and the hydraulic control machinery industry. Due to its numerous appealing features, such as its low complexity, strong resistance to pollutants, and robustness in the face of malfunction, DJSV has attracted a lot of attention since its inception. In 1970, Moog unveiled his two-stage DJSV, which has had a steady rise in popularity ever since. The pilot stage is the essential component of the DJSV. However, many challenges persist owing to the intricate nature of the energy transfer mechanism and the flow field structure. Various academic disciplines have conducted productive research on the DJSV, such as pilot stage modeling, flow force computation, cavitation, and the utilization of innovative materials. Through experimental flow visualization and numerical investigations, B K Saha and Li et al. studied cavitation characteristics in the pilot stage, where bubble shedding or cloud like cavitation is observed and where the significant areas of cavitation were identified [6]. To find out a reasonable flapper shape to reduce the intensity of the cavitation phenomenon, Aung NZ et al. proposed an innovative flapper shape [7]. Using simulated discrete data, Yan et al. developed a 2D model of the pilot stage's internal flow field and determined the steady-state flow force with the help of the momentum principle approach and the differential pressure method [8]. D K Sangiah and Y C Zhu, using the bimorph rectangular actuator and the gigantic magneto constrictive actuator, respectively, created the deflector servo-valve and evaluated its static and dynamic characteristics [9]. The modeling of the pilot stage has been an active area of study in the field of DJSV research. Hao et al. established a mathematical modeling for pressure characteristics in the pilot stage using the momentum or Bernoulli's theorem in conjunction with axisymmetric theory of jet [10]; this is intended for the initial stage with a circular guide groove. The rectangular guiding groove of the pilot stage is the target of the second and third types. The second technique uses plane jet theory and parameter correction to model and analyze the flow field without taking into account the impact of the jet pan's thickness. The third technique considers the depth of the jet pan as its thickness and handles the rectangular jet simply because it is a plane jet with that thickness. This is used to describe the pressure and flow characteristics, but it fails to adjust for the jet's entrainment in the third dimension [11]. When it comes to study value, the pilot stage's pressure-flow properties are much more important. These traits are a good way to show both steady and changing success. The current DJSV pilot stage model has some problems, so we made a new one that better matches the real state of the flow field. This was possible by basing our model on the theory of 3D turbulent jets and the momentum conservation theorem. By using numerical integration, we can find out how important structure factors affect both pressure gain and flow gain. In recent years, the deflector jet servo-valve has been used a lot in aircraft and industry. So, it is an important part of servo control systems and vibration engineering. This research creates a model with a rectangular jet structure to correctly show how the flow moves through the deflector jet control valve. A novel deflecting groove structure is created based on a controlling equation to fix the problems with traditional types. Once this controlling equation and flow pattern inside the pilot stage are known, the pressure gain formula for the pilot stage can be found. Then, using the STAR CCM + software, the numerical solution is obtained to determine the different flow pressures for different values. In the previously developed model, the flapper was moved in the direction of left and right. But in our novel model, we rotated the deflector both in clockwise and anti-clockwise directions to see the pressure distribution, velocity distribution, and cavitation. The deflector jet servo-valve's amplifier disk has extremely small and complex dimensions [12]. In recent research on servo-valves, Ren et al. presented a model-based investigation confirming assumptions connecting jet theory with the deflector jet valve's structure [13]. Abdallah et al. analyzed pressure oscillation and structural parameters, emphasizing the impact of inlet pressure on performance [14]. Yan et al. constructed a numerical model for a more accurate understanding of the deflector jet servo-valve's internal characteristics [15]. Additionally, Abdallah and Li investigated erosion phenomena, highlighting concentration at the shunt wedge and offering insights for performance

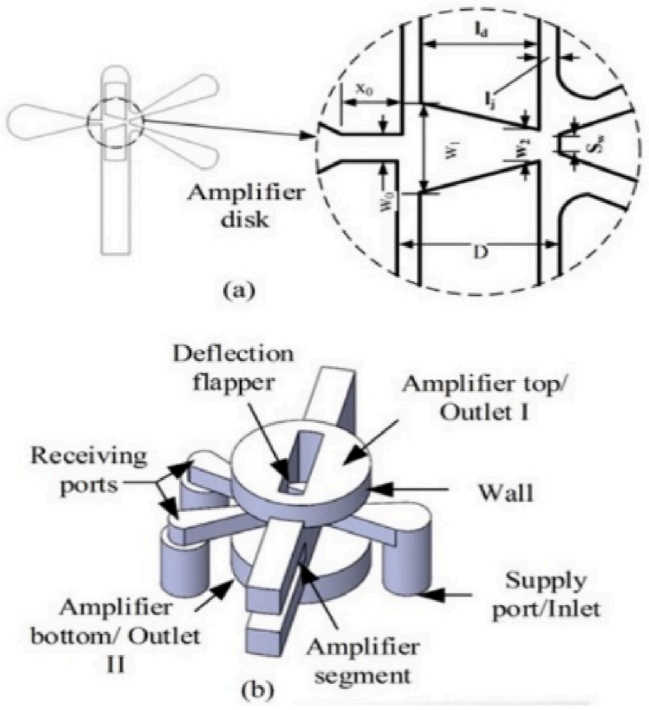

Fig. 2. (a) Amplifier disk of the deflector jet pilot stage and (b) CAD model of deflector jet pilot valve [6].

Table 1
Detail dimensions of the amplifier disk of the deflector jet pilot stage [6].

Symbol	Parameters	Value
D	Distance from the supply nozzle exit to receiving ports	0.86 mm
l_j	Width of null clearance	0.11 mm
l_d	Width of deflector flapper	0.64 mm
S	Width of the splitting wall of receiving ports	0.10 mm
w_0	Width of the supply nozzle exit	0.15 mm
w_1	Width of the flapper groove entrance	0.52 mm
w_2	Width of the flapper groove exit	0.14 mm
x_0	Virtual origin	0.33 mm

improvement [16]. Chu et al. proposed a method for analyzing performance degradation characteristics caused by oil contamination, combining theoretical analysis with multi-physics simulation correction [17]. For enhancing dynamic performance of the jet-pipe servo-valve, Chen et al. introduced a mathematical model and a hierarchical encourage particle swarm optimization genetic algorithm [18]. Another study by Chu et al. focused on the dynamic erosion wear characteristics of a nozzle flapper pressure servo-valve in aircraft brake systems [19]. Finally, Yan et al. conducted a numerical investigation of erosion wear in the hydraulic amplifier of the deflector jet servo valve, proposing a failure criterion and lifespan prediction formula based on contamination levels in hydraulic oil [20]. However, some related research can be found in Refs. [21–25].

In this study, the main objective of this research is to understand the pressure characteristics in the null clearance and receivers, to reduce cavitation by using innovative deflector deflections. We will compare numerically calculated results with traditional models to see how the pressure distribution, velocity distribution, and cavitation differ for different angles of the deflector. Thus, our research focuses on the following topics: optimizing the performance of servo-valves and developing a simple yet effective structure for the amplifier disk, analyzing the velocity distribution by using traditional deflector shapes and innovative deflector shapes, reducing cavitation to ensure enhanced performance, extended component life, noise reduction, and minimal heat generation, and making it beneficial for both customers and manufacturers by ensuring less complicated and more affordable methods of producing deflector jet servo-valves.

2. How does deflector jet servo-valve work?

2.1. Traditional model

A two-stage deflector jet servo-valve usually includes two stages: the main stage and the pilot stage, as shown in Fig. 1. A motor that generates electromagnetic torque is used in the pilot stage. During the initial phase, the amplifier jet disk is stationary or stable. A deflective flapper, equipped with a V-shaped groove that guides, is accurately positioned between two receiving ports and the supply nozzle. Fig. 1 depicts a detailed picture of the deflection flapper and amplifier disk. The application of a low electrical current used to generate an electromagnetic torque motor, although to a small angle, leads the flapper to rotate. The fixed inlet emits fluid through a jet, and that jet is directed to one of the two receiving ports by the flapper groove. Consequently, the accumulation of pressure in the receiving port generates a difference in pressure across the main spool, which in turn drives the spool in the opposite direction of the flapper's motion. Assembling a force balance entails connecting the flapper to the spool via the feedback rod [11].

2.2. Innovative model

The valve's components include a rotary actuator, rotary wheel, rotary flapper, receiver ports, and a supply nozzle. A rotary actuator is a motor that creates electrical torque to enable rotational motion. The rotary disc is similar to the jet disc, except it rotates. The V-shaped, grooved rotary flapper revolves at a particular angle. The receiver ports and supply nozzles are positioned to connect to the rotatable plate. Initially, the revolving wheel and flapper are in a neutral position, with the flapper centred between the receiver locks. The water supply properly mirrors the flow via the flapper groove. When energy is introduced to the motor, an electrical torque is created, forcing the spinning flapper to revolve between −5 and 5°. As the revolving flapper moves, a V-shaped groove sends the fluid to one of two receiving ports. This pressure differential causes the main spool to travel in the opposite direction as the flapper rotates. The spool moves and regulates the flow in the valve's primary stage, resulting in the desired function. A feedback rod links the spinning flapper to the spool, ensuring that the flapper's rotation position corresponds to the position of the spool. This balances the forces and ensures accurate control. Rotational motion causes less harm than linear displacement. It improves control precision over a narrow angular range and enables the construction of compact, durable systems that meet application requirements.

3. Implementation of CFD analysis

3.1. Geometric model simplification

The flow channel in the first stage of the servo-valve has an intricate structure, as seen in Fig. 2.

The dimensions of the amplifier disk for the study of this paper are shown in Table 1 [6].

To boost computational efficiency and save memory, the simulation domain is confined to the closest portion of the pilot stage. The model only focuses on the components in close vicinity to the jet region, illustrated in Fig. 3. The conditions for the boundaries of the CFD model are established by importing the computational domain model into the STAR-CCM + CD-adapco CFD scheme, as seen in Fig. 3. The computational domains consist of three different types of boundaries: the inlet, the outlet, and the wall boundary. In our innovative model, the angular displacement of 5° in clockwise and anti-clockwise directions are implemented. In Fig. 3, the comparison of the traditional model and the

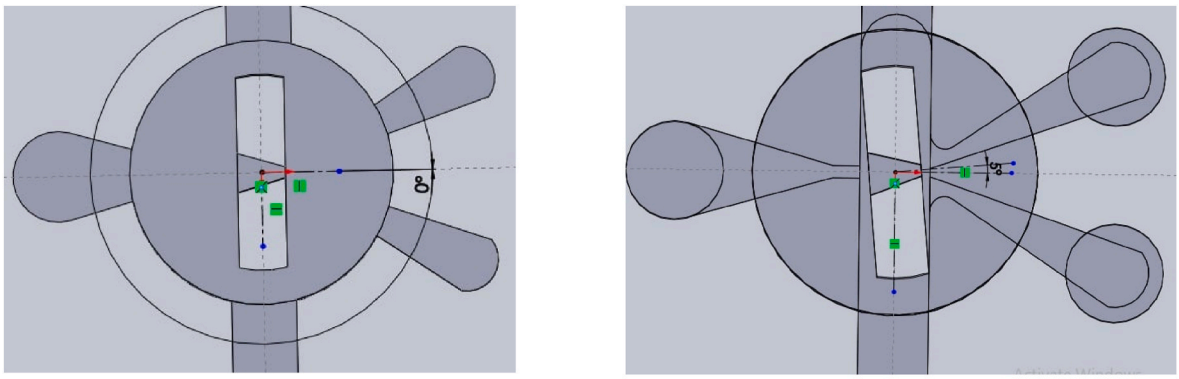

(a) Traditionally used deflector (b) Innovative deflector

Fig. 3. CAD model of deflector.

Table 2
Results of the grid in the dependent test.

Grid	Cells	Faces	Pressure (MPa) in Receiver A	Pressure (MPa) in Receiver B	Mass Flow Rate (Kg/s)
Grid A	323818	954383	4.84	4.89 MPa	4.96e+02
Grid B	363119	1072390	5.01	5.01 MPa	5.18e+02
Grid C	454942	1343081	4.91	4.87 MPa	5.27e+02

innovative model of flapper displacement 5° anti-clockwise is shown.

3.2. Grid independence test

The grid quality in CFD simulations affects the numerical solution of a problem [27]. Using three different grid sizes, namely Grid A, Grid B, and Grid C, grid validation is conducted. It is obvious that there are significant barriers to numerical converges with numerous grids. By using different grides, pressures in receiver A, pressures in receiver B, and mass flow rate at the outlet are computed to inspect the grid dependency of the numerical simulation results, as illustrated in the following Table 2. The relative error between Grid A and Grid B is less than 4 %, while Grid B and Grid C are less than 3 %. In this study, Grid B is selected for the numerical simulations in order to find a balance between computational cost and numerical accuracy.

3.3. Grid distribution

In grid distribution, trimmer, surface remesher, and inflation/prism layer meshing models are applied for generating mesh after importing a 3D model into the Star-CCM + program. Also, we have taken a block part with a thinner base size of 0.00002 *m* and two prism layers. For a more precise meshing, the area close to the flapper's V-groove was considered for refined meshing. There are 363119 cells, 1072390 faces, and 400130 vertices, as shown in Fig. 4.

The convergence accuracy is 1×10^{-5}. Using the mesh of prism layer in combination with the core volume mesh allows for the generation of orthogonal prismatic cells next to wall borders. One of the main ways to evaluate the quality of a mesh system is by looking at its maximum skewness angle. In STAR-CCM+, a skewness angle of 90° or more is troublesome; this may happen in concave cells. Fig. 5 shows that all studies ensure that the highest skewness angle is less than 45°.

3.4. Boundary conditions

The servo-valve structure's boundary conditions are determined according to the shown design in Fig. 2. The computational domains are delineated by three distinct kinds of boundaries: the input, the wall, and

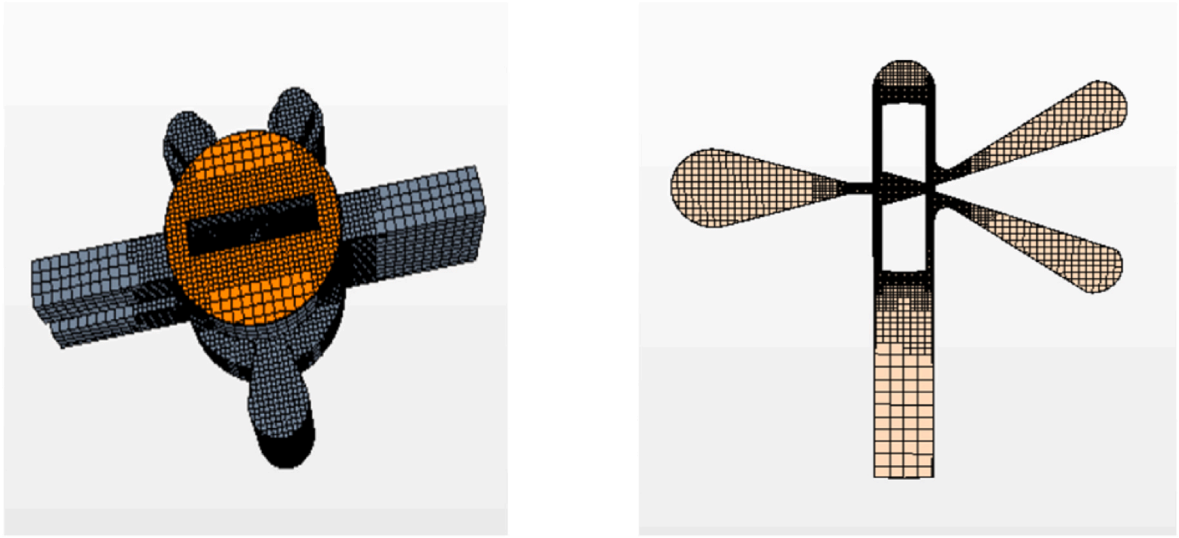

Fig. 4. Mesh model with derived part.

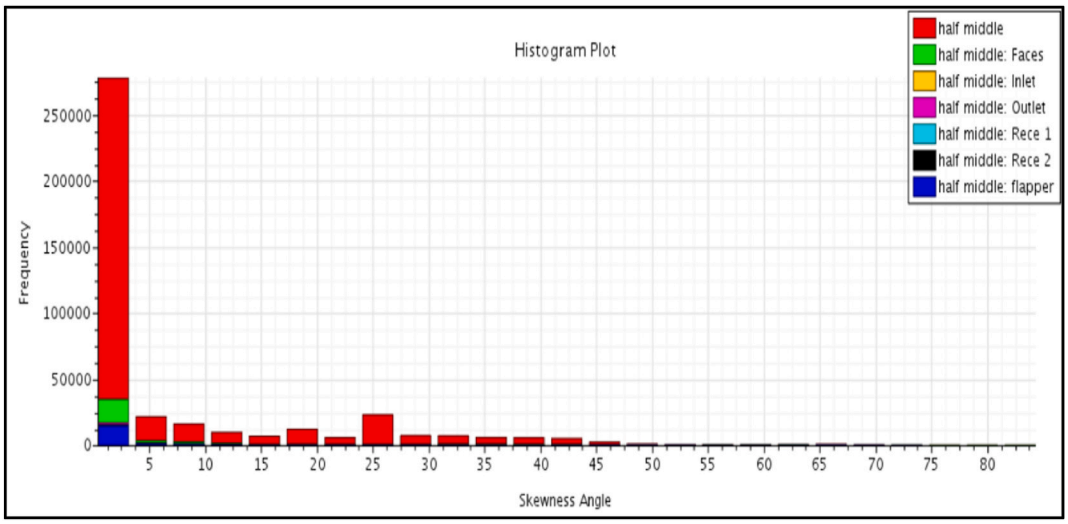

Fig. 5. Histogram plot for skewness angle.

the outlet boundary. The borders that surround the fluid or solid areas are designated as wall-type boundaries on all remaining surfaces. The no-slip condition for wall is inherently enforced in the event of viscous flow. Temperature fluctuations are disregarded. The boundary condition for the inlet pressure is specified as the supply port. The pressure outlet is configured on both the top and bottom sides of the amplifier. The input pressure is 24 MPa, while the output pressure is maintained at 1 MPa.

3.5. Governing equations and solving methods

The physics continua of the STAR-CCM + software takes into account the set of turbulent kinetic energy and dissipation rate equations that are used using a realizable $k-\varepsilon$ model. Mathematical formulations for flow governing equations are:

Continuity equation:

$$\frac{\partial(\rho)}{\partial t}+\nabla.\ (\rho \boldsymbol{u})=0 \tag{1}$$

Momentum transfer equation:

$$\rho\frac{DU}{\partial t}=-\frac{\partial p}{\partial x}+\mu\mathrm{div}(\mathrm{grad}(U))+S_U \tag{2}$$

For in-compressible flow, we have $div(U)=0$, and hence the viscous momentum source terms, S_U for u, v *and* w components are zero. The momentum transfer equation can be expressed as [6,25,28,29]:

$$\frac{\partial(\rho \boldsymbol{u})}{\partial t}+\nabla.(\rho \boldsymbol{u}\boldsymbol{u})=-\nabla p+\nabla.\left[\mu\left(\nabla \boldsymbol{u}+(\nabla \boldsymbol{u})^{T}\right)\right]+\rho \boldsymbol{g}+\boldsymbol{F} +\nabla.\left(\sum_{k=1}^{n}\alpha_k\rho_k \boldsymbol{u}_{dr,\nu}\boldsymbol{u}_{dr,\nu}\right) \tag{3}$$

Where n is phase number, $\boldsymbol{F}$ is body force (N), $\boldsymbol{u}_{dr,\nu}$ is velocity (m/s), α_k is volume fraction of phase k, k is turbulent kinetic energy (J). Thus, the turbulent kinetic energy k and the dissipation rate ε for the Realizable $k-\varepsilon$ model are given as [6]:

$$\frac{\partial(\rho k)}{\partial t}+\nabla.(\rho k\boldsymbol{u})=\nabla.\left[\left(\mu+\frac{\mu_t}{\sigma_k}\right)\nabla k\right]+G_k+G_b-\rho\varepsilon-Y_M+S_k \tag{4}$$

$$\frac{\partial(\rho\varepsilon)}{\partial t}+\nabla.(\rho\varepsilon\boldsymbol{u})=\nabla.\left[\left(\mu+\frac{\mu_t}{\sigma_\varepsilon}\right)\nabla\varepsilon\right]+\rho C_1 S\varepsilon-\rho C_2\frac{\varepsilon^2}{k+\sqrt{\upsilon\varepsilon}}+C_{1\varepsilon}\frac{\varepsilon}{k}C_{2\varepsilon}G_b +S_\varepsilon \tag{4a}$$

where, G_b is Generation of turbulent kinetic energy due to buoyancy, Y_M represents the contribution of the fluctuating dilatation in-compressible turbulence to the overall dissipation rate, $\sigma_k, \sigma_\varepsilon$ represent turbulent Prandtl numbers for k and ε, μ_t is turbulent viscosity of the mixture (N-s/m^2) [6]. Moreover, $C_1=\max\left[0.43,\frac{\eta}{\eta+5}\right]$, $\eta=S\frac{k}{\varepsilon}$, $S=\sqrt{2S_{ij}S_{ij}}$[6]. In Eqs. (4) and (4a), G_k represents the generation of turbulent kinetic energy due to mean velocity gradients, which is calculated as follows: $G_k=\mu_t{}^2S^2$. The terms $\sigma_k=1.0$ and $\sigma_\varepsilon=1.2$ are the turbulent Prandtl numbers for k and ε, respectively.

3.6. Mathematical model for cavitation process

The cavitation model that Schnerr and Sauer created is utilized in the numerical simulations. The following vapor transport equations control the mass conservation equation when cavitation occurs [6,28–30]:

$$\frac{\partial(\alpha\rho_v)}{\partial t}+\nabla.(\alpha\rho_v\boldsymbol{u}_v)=R_e-R_c \tag{5–1}$$

Where, $\boldsymbol{u}_v$ represents velocity of vapor phase (m/s), ρ_v, R_e and R_c represent density of vapor (kg/m^3), vapor generation rate, and vapor condensation rate. Moreover, $\alpha, \rho_v, \mu_v, \rho_l, \mu_l$ represent Volume fraction of vapor, Density of vapor (kg/m^3), kinetic viscosity of vapor, Density of liquid (kg/m^3), kinetic viscosity of liquid respectively. And,

$$R_e=\frac{\rho_v\rho_l}{\rho}\alpha(1-\alpha)\frac{3}{R_b}\sqrt{\frac{2(p_v-p)}{3\rho_l}}\mathrm{if}p\le p_v \tag{5–2}$$

$$R_c=\frac{\rho_v\rho_l}{\rho}\alpha(1-\alpha)\frac{3}{R_b}\sqrt{\frac{2(p-p_v)}{3\rho_l}}\mathrm{if}p\ge p_v \tag{5–3}$$

Where μ_v, ρ_l, μ_l represent kinetic viscosity of vapor, Density of liquid (kg/m^3), kinetic viscosity of liquid respectively. Also p_v represents saturation pressure of the liquid and R_b represents bubble radius. The bubble radius can be expressed as

$$R_b=\left(\frac{\alpha}{1-\alpha}\frac{3}{4\pi}\frac{1}{N_{bubbles}}\right)^{\frac{1}{3}} \tag{5–4}$$

Since the SIMLEC approach permits a higher-pressure correction under the relaxation factor, which helps to speed up convergence, it is employed for the pressure-velocity coupling while solving governing equations [6]. The pressure is handled using the PRESTO! algorithm.

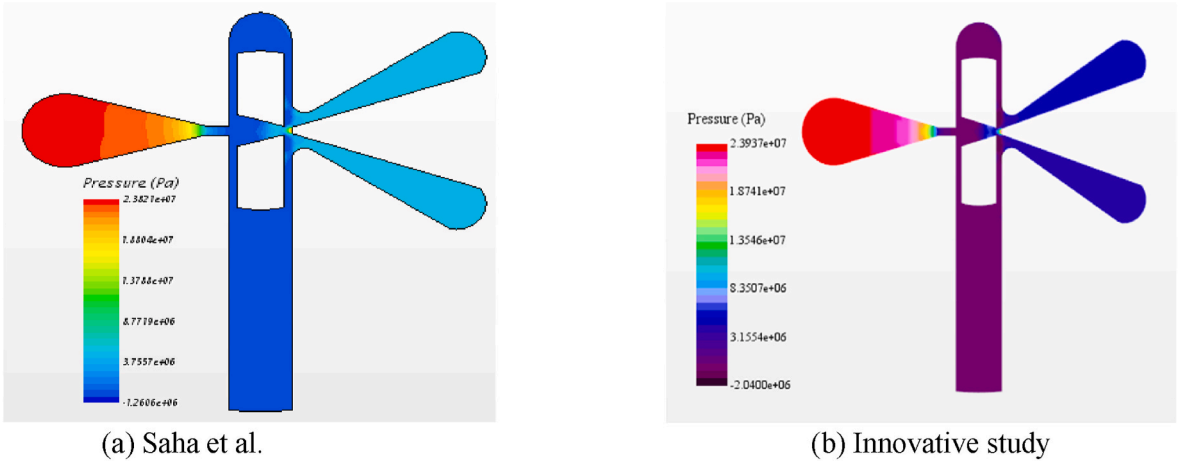

Fig. 6. Comparison of pressure distribution for supply pressure 24Mpa and outlet 0 MPa.

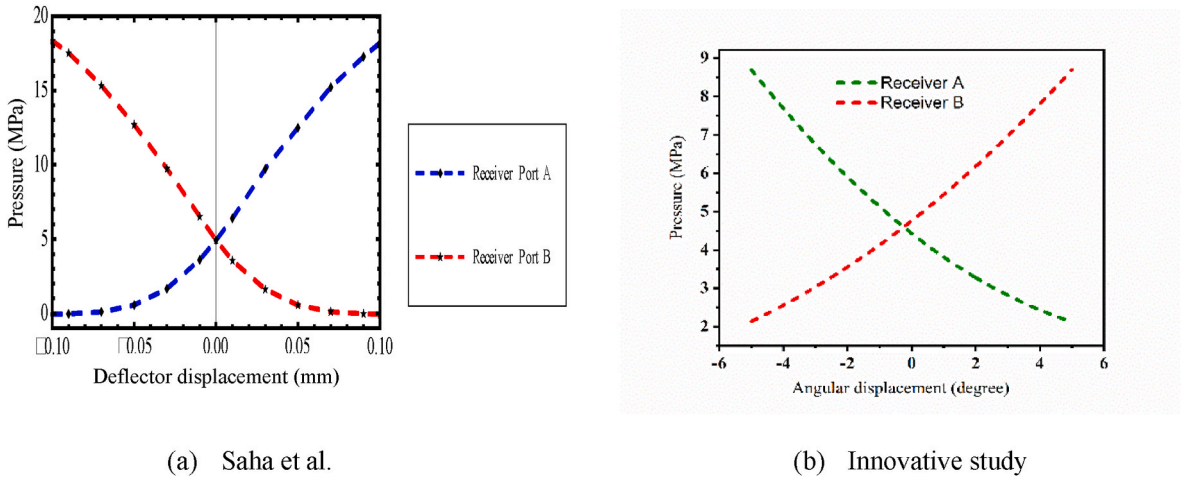

Fig. 7. Comparison of pressure trend of prior model and innovative model for supply pressure 24 MPa and 0 MPa pressure.

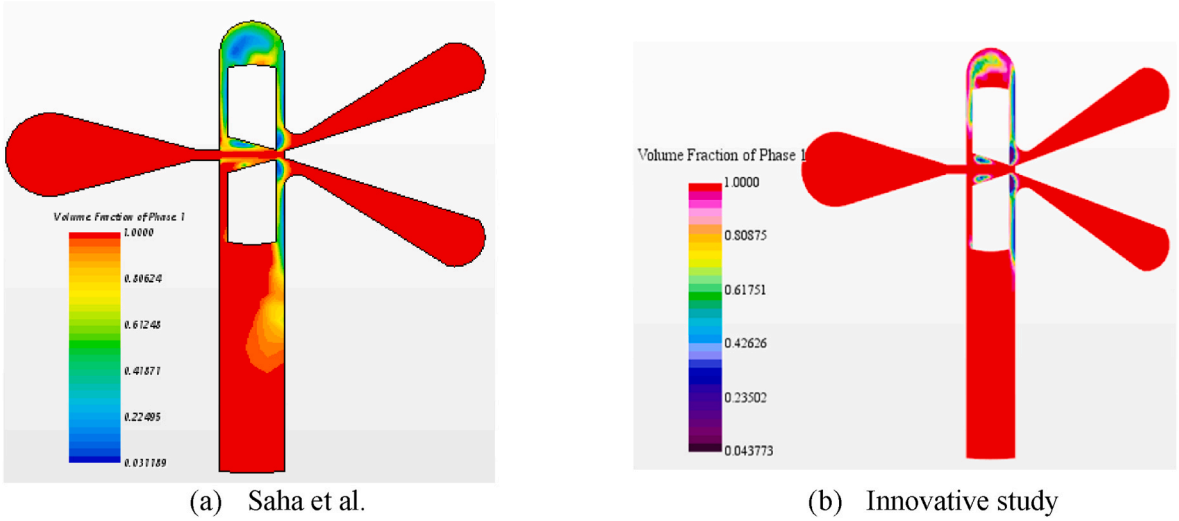

Fig. 8. Comparison of cavitation phenomena of prior model and innovative model.

First-order upwind is applied for momentum, while a second-order technique, called QUICK, is chosen for the volume fraction in order to preserve both accuracy and convergence stability. Oil and oil gas are the main and secondary stages of the interactions, respectively. The results reveal that a vapor volume percentage of 0 represents pure oil, whereas a value of 1 represents pure oil gas. Properties of hydraulic oil are

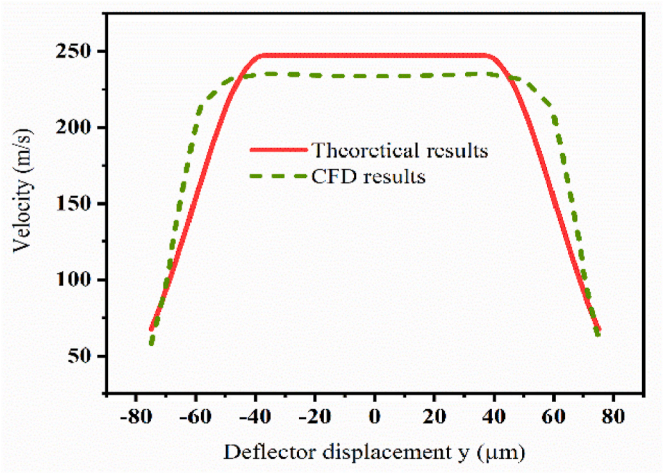

Fig. 9. Comparative study between analytically calculated results with numerical simulations results for velocity distribution of secondary jet at V-groove exit.

considered as density of liquid 850 kg/m^3 , viscosity of liquid 0.0085 $kg/(m\,s)$, Density of vapor 0.025 kg/m^3, Viscosity of vapor $1\times\ 10^{-5}$ $kg/(m\,s)$, Saturation Pressure 3000 Pa [1,11].

3.7. Validation of the CFD model

In order to establish the reliability of our computational approach and verify the accuracy of the accumulated outcomes, a thorough comparison of pressure distribution, cavitation and pressure trend is performed for supply pressure 24 MPa and outlet pressure 0 MPa. The outcomes qualitatively agree with the prior findings by Saha et al. [31]. Initially, the factors that control the pressure changes inside the servo-valve are examined. It is observed that the pressure contour of innovative study is close to the previously developed model by Saha et al. [31] for supply pressure 24 MPa and outlet pressure 0 MPa, where the flapper position is in the middle position, as shown in Fig. 6 (a) and 6 (b). Also, a similar pressure trend is observed for previously developed lateral movement of the flapper and innovative angular movement of the flapper, as shown in Fig. 7 (a) and 7 (b). This comparison of the pressure trends between the traditional model and the innovative model gives a solid base for testing the accuracy of the innovative model by showing how pressures inside the amplifier disk change with the angular movement of the deflector. Moreover, symmetric cavitation is observed in the null clearance for the neutral position of the flapper for both models. In Fig. 8 (a) and 8 (b), it is shown that good agreement is achieved between the prior and present study.

Also, to validate our results precisely, we have compared our simulation results with theoretical results, as shown in Fig. 9. As we know "the maximum velocity of the secondary jet at the V-groove outlet is [32]:

$$u_{s1}=\frac{3u_{s0}}{2+C_1}.\left(\frac{1-\xi_1'}{b_1}\left(y_1+\int_{y_1}^{y_r} exp\left(-\frac{3\left(y-\left(L_{j0}-x_r\right)tan\,\theta_j\right)^2}{\left(y_0-\left(L_{j0}-x_r\right)tan\,\theta_j\right)^2}\right)dy\right)\right)^{1/3}$$

where, u_{s0} is maximum velocity, ξ_1' is "local loss coefficient of fluid flow down the V-groove, b_1 is 0.5 x width of the outlet of the V-groove, y represents the width of the v-groove nozzle exit, y_0 is the distance from the outer boundaries of the first jet to the center line, y_1 is the distance from the inner boundaries of the first jet to the center line, (x_r, y_r) represent stagnation point coordinates, L_{j0} is the potential core length, θ_j is internal spread angle of the first jet, and C_1 represent the dimensionless velocity of the secondary jet at the wall". By comparing theoretical data of the velocity phenomena with simulation data, a good agreement is found, as shown in the following Fig. 9. Finally, it can be concluded that this validation creates good confidence in the present innovative model of angular movement of the flapper to deal with pressure, cavitation, and other phenomena. Therefore, further investigation in this model is possible to conduct.

4. Results discussion

For numerical analysis, the pressure and velocity distributions in receivers are calculated under supply pressure of 24 MPa and output pressure is kept at 1 MPa for varying different displacements of the deflector jet. The volume fraction for oil and air is also calculated numerically. The displacement of the flapper is from anti-clockwise 5° to clockwise 5°.

4.1. Pressure distribution

The modification of the servo valve's flapper to introduce angular movement within a range of −5°–5° has a significant impact on pressure distribution within the system. The precise control of pressure distribution is central to the performance and efficiency of fluid control systems, and this innovative design addresses this critical aspect in a novel way. In traditional servo valves with lateral flapper movement, the pressure distribution is primarily influenced by the linear position of the flapper. As the flapper moves left to right, it controls the orifice size, thereby regulating the flow of fluid and the pressure drop across the

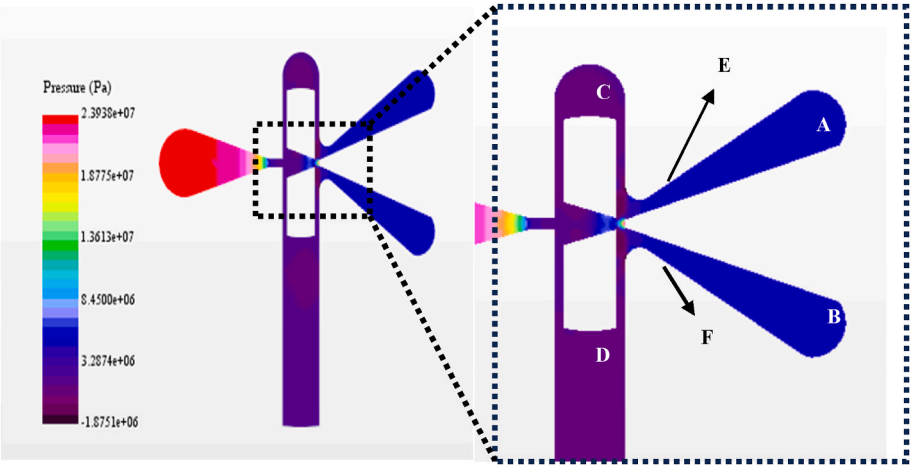

Fig. 10. Pressure distribution inside the pilot for 24 MPa supply pressure.

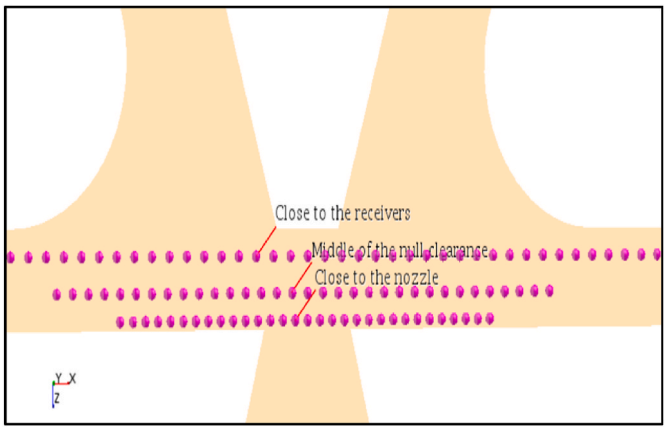

Fig. 11. Line probe in the null clearance.

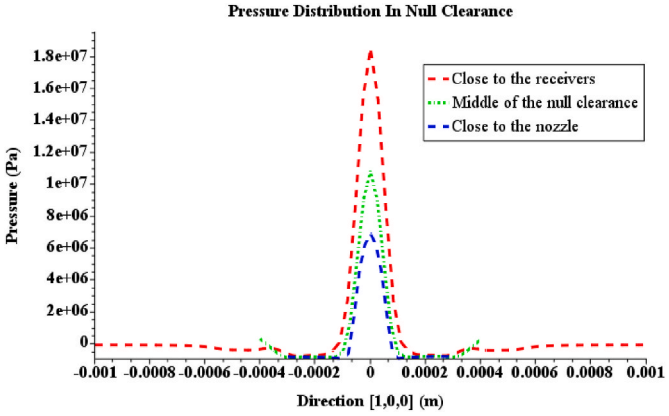

Fig. 12. Pressure distributions at the line probe for 24 MPa supply pressure.

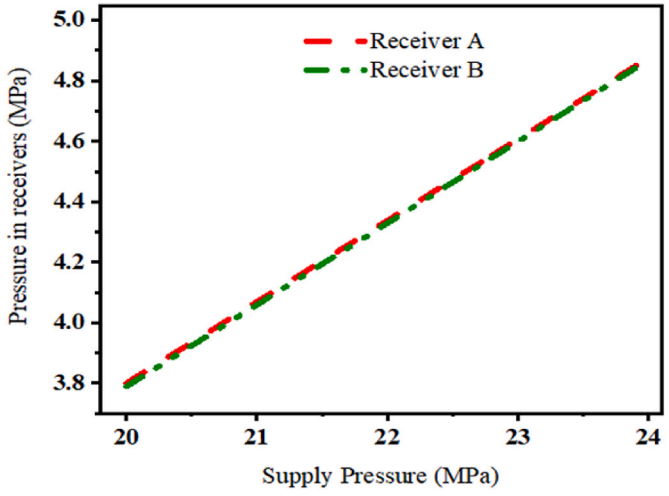

Fig. 13. Pressure in receivers for different supply pressures.

valve. However, this design often encounters challenges related to hysteresis and precision, as the lateral movement may be subject to friction and delayed response. In our innovative design, the introduction of angular flapper movement presents an alternative approach to pressure control. This angular movement allows for a more continuous and dynamic adjustment of the effective orifice area. As the flapper rotates within its specified range, the deflector size varies in a non-linear fashion, which directly impacts the pressure distribution. This design offers the promise of reduced hysteresis, a common challenge in traditional servo valves. Hysteresis is the lag in response observed when the valve's flapper has to overcome static friction before changing position. By minimizing friction through angular movement, this design can lead to more immediate and accurate pressure adjustments, ensuring a more precise response to control inputs.

When the deflector is positioned at the null position without any rotation, it is noticed that the pressure distribution on the receiving ports A and B is identical. Fig. 10 illustrates this behavior. The simulation reveals that the radial-jet flow originating from the deflector nozzle came into contact with the housing wall of the receiving ports A and B. Afterwards, the flow redirected towards the curved surface areas E and F, where it efficiently converted the kinetic energy of hydraulic oil into pressure energy. A portion of the fluids is diverted towards regions C and D as they approach the end of the curved areas E and F. For the closer view, three-line probes, close to the receivers, at the middle of the null clearance, and close to the deflector jet nozzle, are taken to analyze the pressure distribution more frequently, as shown in Fig. 11.

From the following Fig. 12, it is clear that a high-pressure zone is created at the splitting wall of the receivers for the supply pressure of 24 MPa and outlet pressure of 1 MPa. On the other hand, the pressure becomes lower at the deflector jet nozzle tip, which results in cavitation due to the pressure drop.

This results in an even distribution of the increased supply pressure across both sides of the null clearance. Fig. 13 reveals that when the defector jet is in the middle position, pressure in two receiving ports increases simultaneously for the increment of supply pressure from 20 MPa to 24 MPa.

Notably, depending on the design and configuration of the hydraulic system, the precise behavior of a servo-valve system may vary. Variations in hydraulic circuit design, the type of servo valve, and the feedback mechanism can all impact the process in which changes in supply pressure occur in different parts of the system. One crucial aspect of this innovation lies in its impact on pressure distribution within the valve and receivers A and B. To understand this impact, we need to explore the intricate relationship between the angular flapper movement and pressure distribution at different stages of the valve's operation.

As the flapper moves from its initial -5-degree position towards the neutral position, the effective orifice size gradually decreases, leading to a reduction of pressure drop in receiver A and an increase in receiver B. Further, when the flapper reaches its 5-degree position from the neutral position, the orifice area is at its maximum, and opposite phenomena occur. Receivers A and B of the servo-valve experience distinct pressure profiles based on the different angular positions of the deflector. Receiver A will initially have a higher pressure due to the initial -5° flapper position, and receiver B will have low pressure, as shown in Fig. 14 (a). As the flapper moves towards its neutral position, the pressure in receiver A gradually decreases. as shown in Fig. 14 (a) to 14 (e).

Fig. 14 (f) shows the pressure distribution in the neutral position, and it is observed that at the null position, without rotating the deflector, the distribution of the pressure on the receiving ports A and B is the same. When the flapper reaches its 5-degree position, receiver A experiences the highest pressure, corresponding to the maximum pressure across the valve. In contrast, receiver B will receive a lower pressure than receiver A as shown in Fig. 15.

Considering all the above facts together, by varying the deflector's position within the range of -5°–5°, pressure recovery on two ports can be calculated. As the deflector rotated anti-clockwise, the pressure in port A exhibited a significant increase, reaching a peak pressure of 8.919404 MPa, as the deflector nozzle area is exactly over the left receiver ports. Further, pressure in the receiver port B decreased, ultimately attaining a minimum pressure of 3.723784 MPa. In the middle position, both receivers receive the same pressure of 5.01 MPa. While the deflector rotated clockwise, port A receives a maximum pressure of 8.918744 MPa, while a decreased pressure of 3.872334 MPa pressure is received in port B. This phenomenon is shown in Fig. 15.

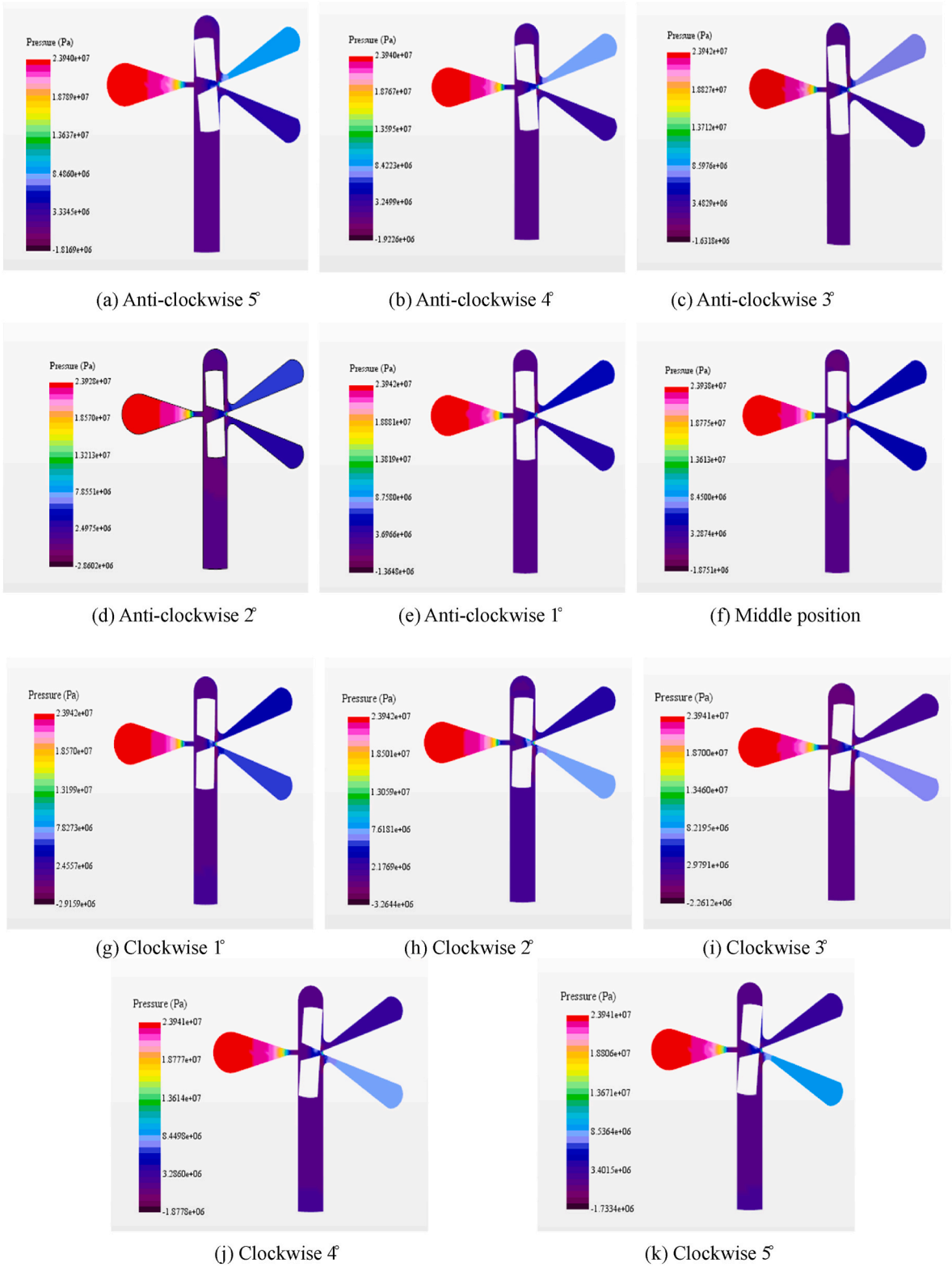

Fig. 14. Pressure distribution for the different flapper positions.

Finally, according to the above discussion, it is obvious that the pressure distribution in receivers A and B can be described as the function of the angular position of the flapper. The control and precision offered by this angular flapper movement design have the potential to improve the overall performance of the fluid control system significantly.

4.2. *Velocity distribution*

As the supply pressure is 24 MPa, therefore the flow is considered turbulent. The scalar and vector contours for the neutral position of the flapper are shown in Fig. 16 (a) and (b). The analysis of the simulated flow field shows that turbulent flow comes from the exit of the supply

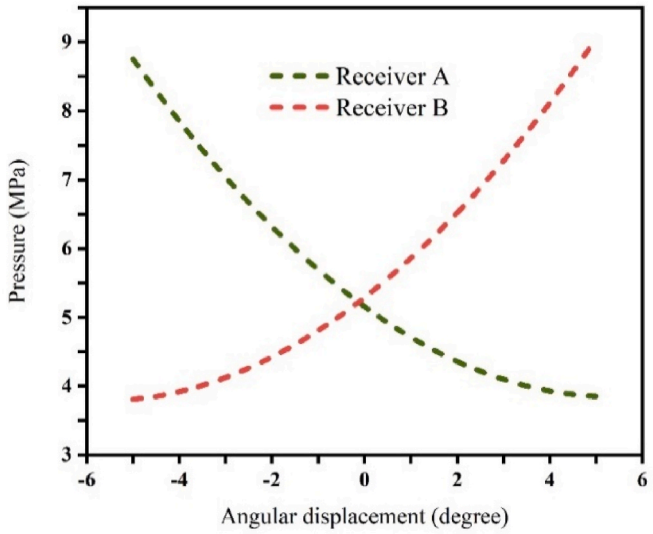

Fig. 15. Pressure distribution in two receiver ports A & B for the innovative model.

nozzle and proceeds towards the flapper groove, ultimately impinging onto the flapper groove lateral wall. Simultaneously, The fluid's contact with the lateral walls of the flapper groove causes momentum downstream flow as well as back-flow within the groove. The vortex formation in the flapper groove is symmetrical along the center line. The creation of vortex vector lines at points G and H are shown in Fig. 16 (b). The cavitation forms as a result of a pressure drop caused by the vortex inside the flapper groove.

Following a collision with the side wall of the flapper, some of the fluid flows along the lateral wall to the flapper groove exit. The fluid particles exiting the flapper groove at a high velocity clash with the splitting wall of the receivers and return to regions E and F. After getting close to the end of the bent regions E and F, fluid flow proceeds towards the regions C and D and reaches the outlet. The analysis of the velocity in the null clearance, which is a region of significant importance in this servo-valve model, is particularly challenging and critical. This is

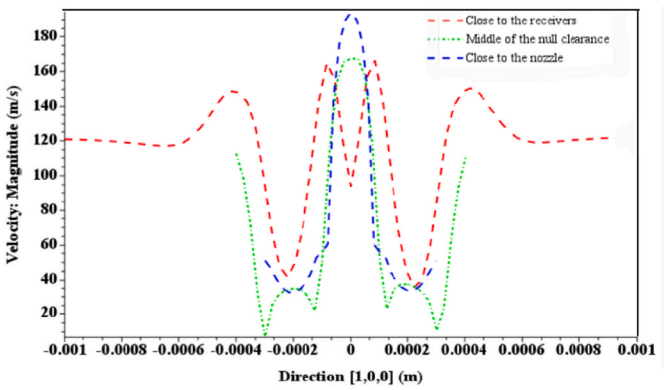

Fig. 17. Velocity distributions for 24 MPa supply pressure at the line probe.

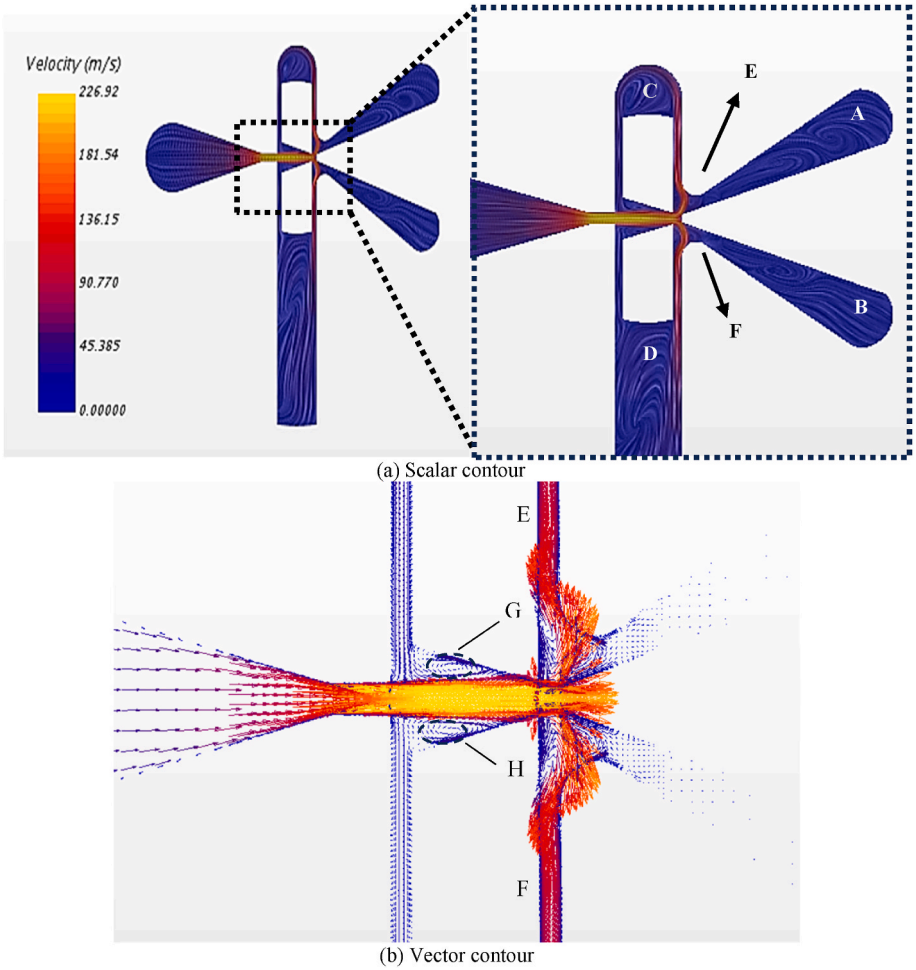

Fig. 16. Velocity distribution for supply pressure 24 MPa.

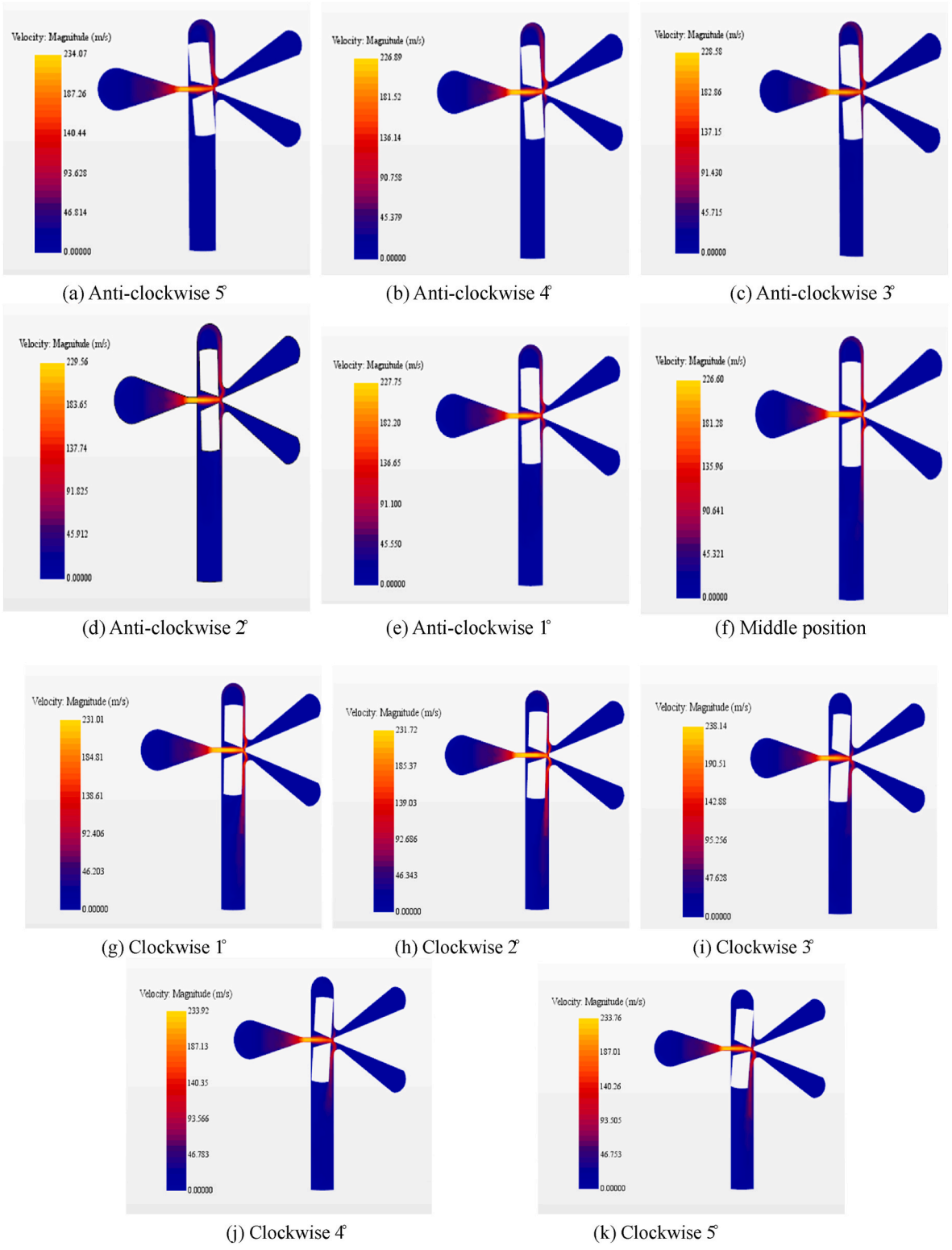

Fig. 18. Velocity distribution for the different flapper positions.

attributed to the unconventional angular movement of the flapper in this innovative model. In contrast to conventional linear flapper movements, the angular rotation of the flapper introduces a variable gap between the flapper and the orifice. This variation in gap size affects the flow resistance and, as a result, the velocity distribution within this critical clearance. In the neutral position, where the flapper is set at zero degrees, the velocity distribution in both the null clearances remains the same, as shown in Fig. 16.

In terms of boundary layer effects and turbulence, the neutral position experiences reduced turbulence compared to the -5-degree position. The fluid flows more smoothly due to the balanced flow conditions, resulting in a more uniform velocity distribution within both sides of null clearance. The absence of significant flow restrictions or expansions contributes to a more predictable and stable flow profile. To understand

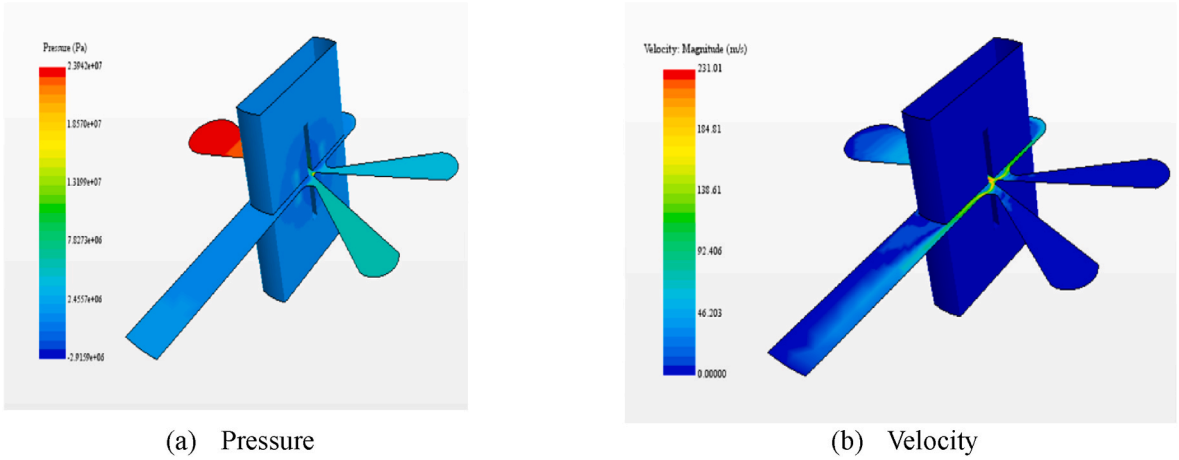

Fig. 19. Pressure and velocity in the cross-sectional area.

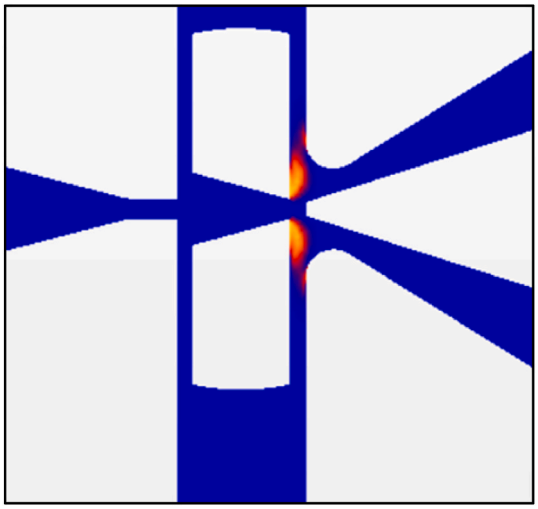

Fig. 20. Volume fraction of air.

the velocity phenomena in null clearance more precisely, three-line probes, close to the receivers, at the middle of the null clearance, and close to the nozzle, have been taken have been taken and the results are shown in Fig. 17.

From this figure, it is clearly visible that velocity is higher in the area close to the nozzle. To understand the velocity distribution more precisely, velocity distribution for different flapper position has been analyzed shown in Fig. 18. For getting a clear overview of flow filed, the pressure and velocity of the cross-sectional area has been observed as shown in Fig. 19.

4.3. Cavitation

Cavitation is the formation of vapor-filled cavities in a liquid owing to a decrease in pressure below the vapor pressure, followed by a rapid acceleration. Nevertheless, a novel approach has been implemented, where the flapper is subjected to rotational movement within an angular region ranging from −5° to 5°. As the flapper rotates within its angular range, it affects the null clearance. The changing geometry and flapper movement cause variations in pressure and flow. This analysis aims to investigate the phenomenon of cavitation under specific conditions, where the supply pressure is taken 24 MPa, and the outlet pressure is employed 1 MPa. In the neutral position of the servo-valve, where the flapper is neither rotated clockwise nor anti-clockwise, the fluid experiences a more stable and symmetric pressure distribution. At this point, the fluid undergoes acceleration as it navigates through the valve system, and any localized pressure drops within the null clearance can potentially lead to cavitation events as shown in Fig. 20. The physics of cavitation in the neutral position revolves around pressure differentials and the potential for vapor bubble formation. As the fluid accelerates and encounters the null clearance, pressure changes occur. If these pressure drops reach a critical point, they can induce the formation of vapor bubbles. It's important to note that the absence of flapper rotation simplifies the fluid dynamics at play but doesn't eliminate the possibility of cavitation. In the neutral position, the risk of cavitation is generally more dependent on the specific design parameters, such as the geometry of the null clearance and the supply pressure magnitude. Cavitation events in the neutral position may manifest as localized pressure drops, leading to the formation of small vapor bubbles. The subsequent collapse of these bubbles, though less influenced by rotational dynamics, can still generate shock waves and contribute to erosion and pitting on the surfaces of the valve components.

The phenomena of cavitation can be widely described by volume fraction. When the flapper is positioned at −5°, the asymmetrical opening and blocking of fluid pathways induce a localized increase in fluid velocity within the null clearance region around receiver A. This acceleration of fluid creates a reduced pressure zone in the vicinity of receiver A.

The angular displacement of the flapper at −5° generates a low-pressure zone in receiver A, promoting the initiation of cavitation. Conversely, in receiver B, the fluid pathways experience less obstruction, limiting the increase in fluid velocity. Consequently, the low-pressure zone in receiver B is less pronounced compared to receiver A, resulting in a lower incidence of cavitation. This is shown in Fig. 21 (a). As the is moved towards the neutral position, the velocity distribution in receiver B reduces, and increasing velocity is introduced in receiver A, as shown in Fig. 21 (a) to 21 (e). At the neutral position, where the flapper is in the middle position, the system reaches a state of equilibrium. The fluid velocities and pressure differentials stabilize, leading to a reduction in the low-pressure zone in both receivers A and B. The symmetrical structural shape of cavitation observed at this point reflects the balanced interaction between the flapper and fluid, minimizing the creation of significant low-pressure regions, as shown in Fig. 21 (f). As the flapper progresses to 5°, a reverse scenario occurs. The angular displacement now creates a more obstructed pathway in receiver A, elevating fluid velocity and, consequently, reducing pressure. This induces a low-pressure zone in receiver A, promoting the initiation of cavitation. Simultaneously, in receiver B, the less obstructed fluid pathway results in a lower low-pressure zone, leading to a reduced occurrence of cavitation compared to receiver A. This phenomenon is shown in Fig. 21 (g) to Fig. 21 (k). Therefore, we can conclude that the creation of a low-

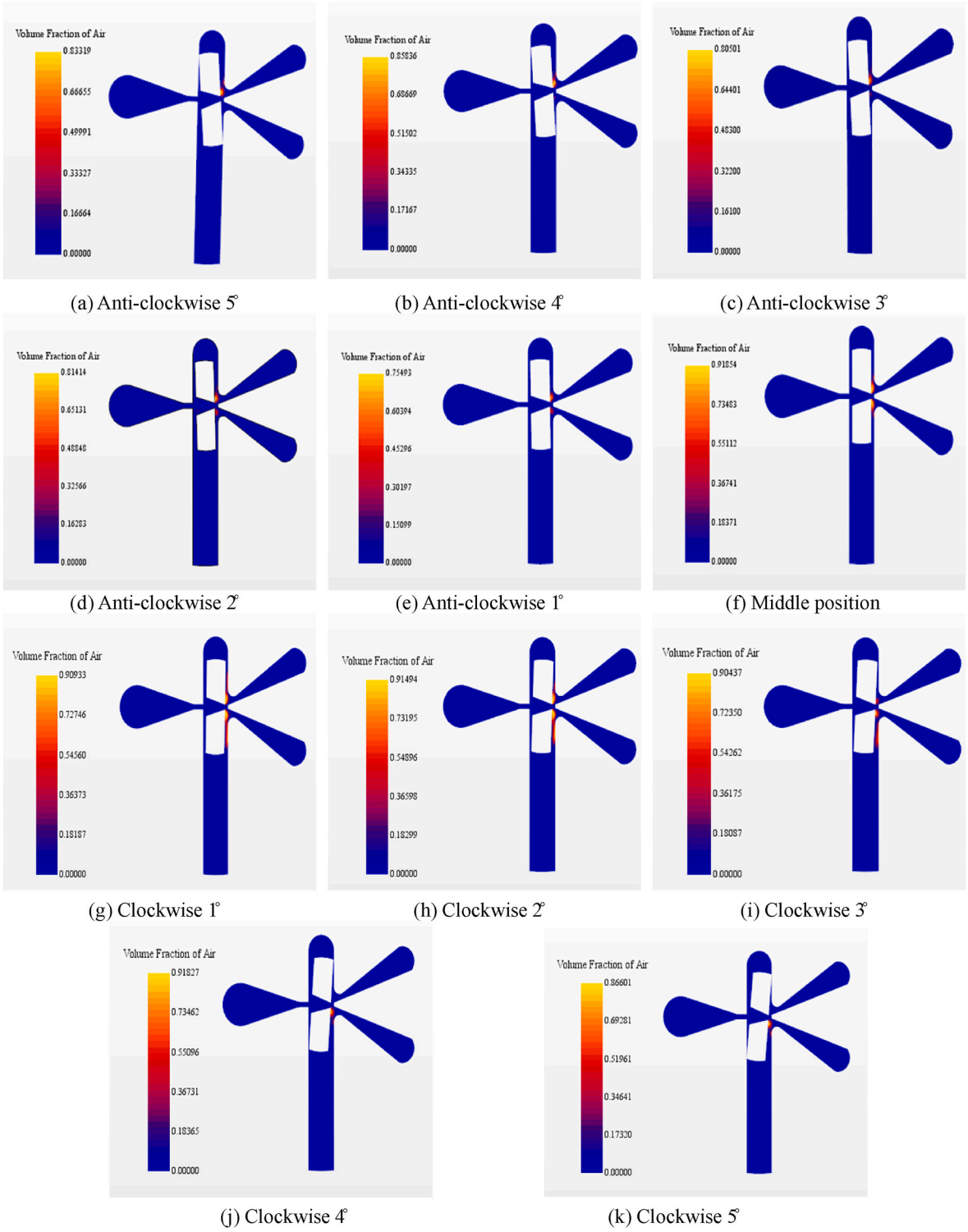

Fig. 21. Volume fraction of air for the different flapper positions.

pressure zone is intricately linked to the fluid dynamics induced by the angular movement of the flapper. The interaction between fluid velocity, pressure differentials, and the geometry of the servo-valve system gives rise to localized pressure variations, shaping the occurrence and intensity of cavitation in receivers A and B at different flapper positions. Moreover, the implementation of a new innovative model in servo-valve design has yielded a notable reduction in cavitation compared to traditional models featuring linear left-to-right flapper movement. This achievement can be attributed to several key factors inherent to the novel design.

In Fig. 22 the comparison of cavitation phenomena between traditional left/right 0.05 mm and innovative anti-clockwise/clockwise 5° are shown to understand the difference between traditional and innovative model. The angular flapper rotation, as opposed to the traditional linear movement, optimizes fluid dynamics within the null clearance region. By allowing a more controlled and gradual modulation of fluid flow, the new model minimizes abrupt changes in fluid velocity that often trigger cavitation in conventional designs. The smoother transition

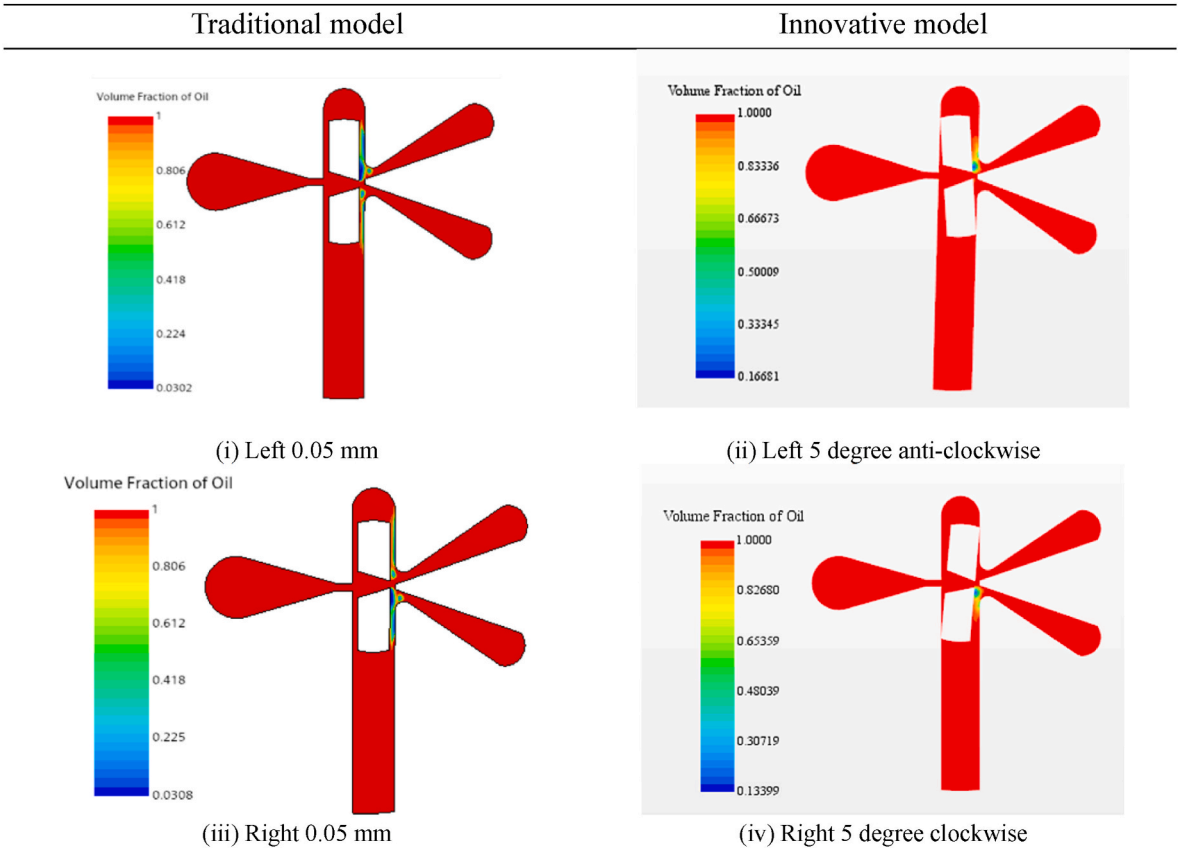

Fig. 22. Comparison of cavitation phenomena between traditional and innovative model for varying the deflector displacement.

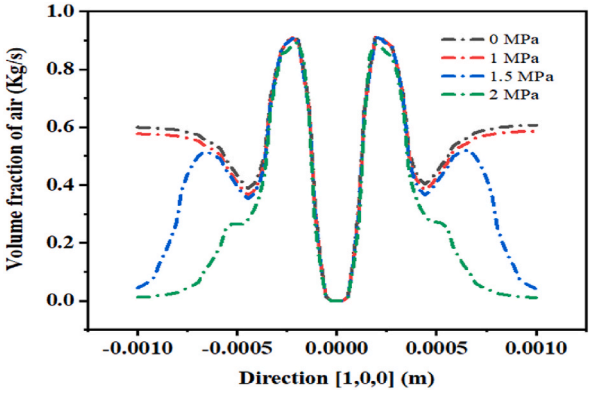

Fig. 23. Volume fraction of air for outlet pressure 0 MPa, 1 MPa, 1.5 MPa and 2 MPa.

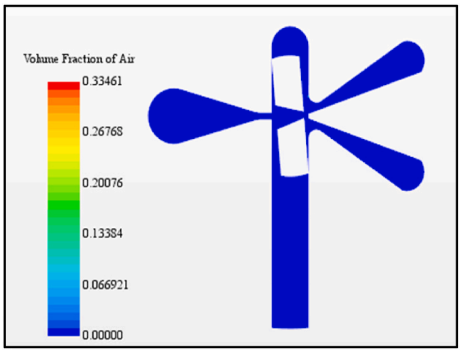

Fig. 24. Cavitation phenomena for outlet pressure 1.5 MPa.

facilitated by angular rotation mitigates the formation of low-pressure zones.

Further, to analyze the cavitation phenomena more deeply, the volume fraction of air is calculated at the line probe near the flapper groove exit for outlet pressures 0 MPa, 1 MPa, 1.5 MPa and 2 MPa. It is observed that cavitation is reduced for the increase of outlet pressure [33]. In our study, this phenomena are shown in Fig. 23.

Moreover, by increasing the outlet from 1 MPa to 1.5 MPa it is observed that the cavitation reduces, as shown in Fig. 24. Increasing the servo valve's outlet pressure can effectively reduce the risk of cavitation, safeguard the valve from damage, and improve its performance by reducing the creation and increasing the collapse of vapor bubbles. The bubbles implode with greater force because the increased pressure

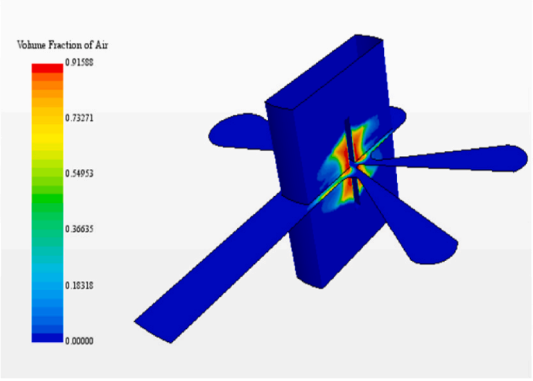

Fig. 25. Volume fraction of air in the cross-section area.

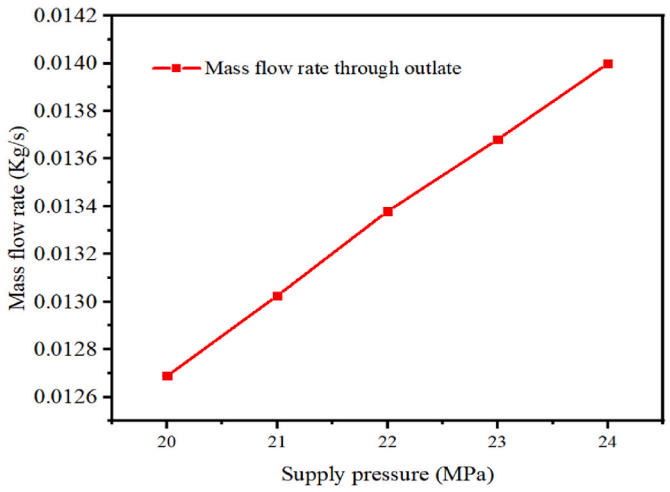

Fig. 26. Mass flow rate for different supply pressures.

around them acts as a greater barrier to their expansion. Even though this violent bubble collapse can still cause vibration and noise, it lessens the erosional consequences of cavitation, which can harm valve components.

The physics is observed for the increase in mass flow rate through the outlet as the supply pressure escalates from 20 MPa to 24 MPa. For getting further overview the volume fraction of air has been observed as shown in Fig. 25.

As the supply pressure is increased, the potential energy of the fluid is raised, leading to an increase in kinetic energy at the outlet. The mass flow rate of the innovative model for different supply pressures is shown in Fig. 26.

5. Limitations

Rotational models add mechanical complexity owing to the necessity for precise angular control. The sensitivity and torque production of the servo motor make designing and manufacturing parts for these models difficult. Variations in torque have the potential to cause inaccurate valve location, which would impair system performance. While rotating motion reduces wear, it can also cause wear over time, necessitating more maintenance. Little angular range restricts motion and control range, which can lead to greater displacements or wider control ranges. The inertia of rotating components may cause rotational models to respond more slowly than other models. It can be difficult to implement exact feedback mechanisms for precise rotary flapper positioning. Furthermore, a rotary flapper misalignment can result in inaccurate pressure differentials, lower valve performance, and inaccurate fluid jet direction due to an unmeasurable translational installation bias.

6. Conclusion

Aiming to reduce undesired flow phenomena inside the deflector jet pilot valve, innovative deflections of deflector are proposed in this research. The numerical analysis is performed by using the commercial computational fluid dynamics software STAR CCM+. Finally, from our results and discussions, the following conclusions are made:

1. The numerically calculated results are compared with traditional deflector jet models to see how the velocity, pressure, and cavitation distribution differ for varying angles of the deflector. The result shows that by the innovative rotation of the deflector both in clockwise and anti-clockwise directions, significant pressure in the receivers is obtained than traditionally moving deflector to the left and right for the same supply pressure. The displacement of the deflector is from anti-clockwise 5° to clockwise 5°. Moreover, when the deflector is positioned clockwise or anti-clockwise by 5°, less cavitation is observed than in the traditional model. At the neutral position, where the flapper is in the middle position, the attached like cavity can be seen both sides of the deflector jet nozzle tip.
2. The profile of pressure, and vapor volume fraction distributions at the narrow region of null clearance inside the deflector jet pilot stage confirm that cavitation is caused by turbulent pressure fluctuations and high velocities at the sharp edges of the deflector groove exit tip. The outcomes demonstrate that the novel deflector deflection will be a wise decision in lowering the degree of cavitation and flow-induced phenomena. Conversely, by manipulating the flow direction along the null clearance, the deflector's novel rotation lessens the cavitation intensity.
3. When the flapper is rotated from a neutral position to either Anti clock-wise or clock-wise 5-degree position, the pressure in receiver A again increases gradually, and the pressure in receiver B decreases vice versa. It is observed that the pressure trend of the innovative deflector deflection model is similar as the traditional model.
4. It is also feasible to draw the conclusion that, while the cavitation reduction effect is noteworthy, the increase in output pressure to 2 MPa has no discernible impact on the mass flow rate trend at the deflector jet pilot stage's outlet. Eventually, the novel deflector deflection's ability to lessen cavitation intensity and improve performance overall is demonstrated.
5. Despite the fundamental difficulties, the innovative deflector deflection model is proposed in this research, along with its numerical implementation, can be considered dependable and beneficial for enhancing the performance of the deflector jet servo-valve in future design endeavors.

CRediT authorship contribution statement

Jinghui Peng: Writing – review & editing, Visualization, Validation, Supervision, Investigation, Formal analysis. **Bijan Krishna Saha:** Writing – original draft, Visualization, Validation, Supervision, Software, Project administration, Investigation, Funding acquisition, Formal analysis, Conceptualization. **Md Shah Najmus Shakib:** Writing – original draft, Visualization, Validation, Software, Methodology, Investigation, Formal analysis. **Songjing Li:** Writing – review & editing, Visualization, Validation, Supervision, Project administration, Funding acquisition, Formal analysis, Conceptualization. **Jahidul Islam Jihan:** Writing – review & editing, Visualization, Validation, Software, Methodology, Investigation, Formal analysis.

Declaration of competing interest

The authors declare that they have no known competing financial interests or personal relationships that could have appeared to influence the work reported in this paper.

Data availability

Data will be made available on request.

Acknowledgments

The following support is gratefully acknowledged: The National Natural Science Foundation of China (No. 51675119), The University Grants Commission (UGC) of Bangladesh with Grant No. Source: Engineering Science (Civil, Mechanical and Electrical)-12-2021.

References

[1] A.R. Plummer, Electro-hydraulic servo-valves- past, present, and future, in: 10th International Fluid Power Conference, 2016, Dresden, Germany, 2017, pp. 405–424.

[2] P. Tamburrano, A.R. Plummer, E. Distaso, R. Amirante, A review of electro-hydraulic servovalve research and development, Int. J. Fluid Power (Oct. 2018) 1–23, https://doi.org/10.1080/14399776.2018.1537456.

[3] P. Tamburrano, A.K. Plummer, E. Distaso, R. Amirante, A review of direct drive proportional electrohydraulic spool valves: industrial state-of-the-art and research advancements, J. Dyn. Syst. Meas. Control 141 (2019) 020801.

[4] S. Li, Y. Song, Dynamic response of a hydraulic servo-valve torque motor with magnetic fluids, Mechatronics 17 (8) (Oct. 2007) 442–447, https://doi.org/10.1016/j.mechatronics.2007.04.011.

[5] Z. Peng, C. Sun, R.-B. Yuan, P. Zhang, The CFD analysis of main valve flow field and structural optimization for double-nozzle flapper servo valve, Procedia Eng. 31 (2012) 115–121, https://doi.org/10.1016/j.proeng.2012.01.1000.

[6] B.K. Saha, J. Peng, S. Li, Numerical and experimental investigations of cavitation phenomena inside the pilot stage of the deflector jet servo-valve, IEEE Access 8 (2020) 64238–64249, https://doi.org/10.1109/ACCESS.2020.2984481.

[7] N.Z. Aung, S. Li, A numerical study of cavitation phenomenon in a flapper-nozzle pilot stage of an electro-hydraulic servo-valve with an innovative flapper shape, Energy Convers. Manag. 77 (2014) 31–39.

[8] J. Hu, Z. Yang, Z. Huang, Y. Jin, B. Yu, X. Kong, Flow measurement for the pre-stage of jet pipe servo valve using 2D -PIV technique, Int. J. Fluid Power 19 (3) (Sep. 2018) 165–172, https://doi.org/10.1080/14399776.2018.1514931.

[9] D.K. Sangiah, A.R. Plummer, C.R. Bowen, P. Guerrier, A novel piezohydraulic aerospace servovalve. Part 1: design and modelling, Proc. IME J. Syst. Control Eng. 227 (4) (Apr. 2013) 371–389, https://doi.org/10.1177/0959651813478288.

[10] Y. Li, Mathematical modelling and characteristics of the pilot valve applied to a jet-pipe/deflector-jet servovalve, Sens Actuators A Phys 245 (Jul. 2016) 150–159, https://doi.org/10.1016/j.sna.2016.04.048.

[11] B.K. Saha, S. Li, X. Lv, Analysis of pressure characteristics under laminar and turbulent flow states inside the pilot stage of a deflection flapper servo-valve: mathematical modeling with CFD study and experimental validation, Chin. J. Aeronaut. 33 (3) (Mar. 2020) 1107–1118, https://doi.org/10.1016/j.cja.2019.11.016.

[12] H. Yan, Y. Ren, L. Yao, L. Dong, Analysis of the internal characteristics of a deflector jet servo valve, Chin. J. Mech. Eng. 32 (1) (Dec. 2019), https://doi.org/10.1186/s10033-019-0345-7.

[13] Y. Ren, H. Yan, Q. Mao, Z. Zuo, H. Hao, A model-based investigation of the performance robustness of the deflector jet servo valve, Appl. Sci. 12 (20) (Oct. 2022), https://doi.org/10.3390/app122010428.

[14] H.K. Abdallah, J. Peng, S. Li, Analysis of pressure oscillation and structural parameters on the performance of deflector jet servo valve, Alex. Eng. J. 63 (Jan. 2023) 675–692, https://doi.org/10.1016/j.aej.2022.11.021.

[15] H. Yan, Y. Ren, L. Yao, L. Dong, Analysis of the internal characteristics of a deflector jet servo valve, Chin. J. Mech. Eng. 32 (1) (Dec. 2019), https://doi.org/10.1186/s10033-019-0345-7.

[16] H.K. Abdallah, R. Ben-Mansour, S. Li, Numerical study of erosion phenomena with the presence of cavitation at deflector jet servo-valve, Arabian J. Sci. Eng. (2023), https://doi.org/10.1007/s13369-023-08427-y.

[17] Y. Chu, Z. Yuan, X. He, Z. Dong, Model construction and performance degradation characteristics of a deflector jet pressure servo valve under the condition of oil contamination, International Journal of Aerospace Engineering 2021 (2021), https://doi.org/10.1155/2021/8840084.

[18] J. Chen, F. Li, Y. Yang, Y. Gao, Mathematical modelling and hierarchical encourage particle swarm optimization genetic algorithm for jet pipe servo valve, Comput. Intell. Neurosci. 2022 (2022), https://doi.org/10.1155/2022/9155248.

[19] Y. Chu, Z. Yuan, W. Chang, Research on the dynamic erosion wear characteristics of a nozzle flapper pressure servo valve used in aircraft brake system, Math. Probl Eng. 2020 (2020), https://doi.org/10.1155/2020/3136412.

[20] H. Yan, J. Li, C. Cai, Y. Ren, Numerical investigation of erosion wear in the hydraulic amplifier of the deflector jet servo valve, Appl. Sci. 10 (4) (Feb. 2020), https://doi.org/10.3390/app10041299.

[21] S. Zhang, N.Z. Aung, S. Li, Reduction of undesired lateral forces acting on the flapper of a flapper–nozzle pilot valve by using an innovative flapper shape, Energy Convers. Manag. 106 (2015) 835–848.

[22] S. Li, N.Z. Aung, S. Zhang, J. Cao, X. Xue, Experimental and numerical investigation of cavitation phenomenon in flapper–nozzle pilot stage of an electro–hydraulic servo–valve, Comput. Fluid 88 (2013) 590–598.

[23] H. Yan, Y. Ren, L. Yao, L. Dong, Analysis of the internal characteristics of a deflector jet servo valve, Chin. J. Mech. Eng. 32 (1) (Dec. 2019), https://doi.org/10.1186/s10033-019-0345-7.

[24] Q. Yang, N.Z. Aung, S. Li, Confirmation on the effectiveness of rectangle-shaped flapper in reducing cavitation in a Flapper–Nozzle pilot valve, Energy Convers. Manag. 98 (2015) 184–198.

[25] B.K. Saha, L. Li, S. Li, CFD investigations of flow field and cavitation phenomena in the pilot stage of deflector jet servo-valve, in: AIP Conference Proceedings, American Institute of Physics Inc., Feb. 2019, https://doi.org/10.1063/1.5090679.

[26] N. Liang, Z. Yuan, F. Zhang, Oil particle-induced erosion wear on the deflector jet servo valve prestage, Aerospace 10 (1) (Jan. 2023) 67, https://doi.org/10.3390/aerospace10010067.

[27] A. Katz, V. Sankaran, Mesh quality effects on the accuracy of CFD solutions on unstructured meshes, J. Comput. Phys. 230 (20) (Aug. 2011) 7670–7686, https://doi.org/10.1016/j.jcp.2011.06.023.

[28] N. Mohon, A. Pattamatta, Implementation of two-layer realizable k-ε turbulence model into open-foam for the simulation of nuclear reactor cooling system [C], in: Proceedings of the 23rd National Heat and Mass Transfer Conference and 1st International ISHMT-ASTFE Heat and Mass Transfer Conference, Thiruvananthapuram, India, vol. 981, 2015, pp. 1–8.

[29] H.K. Versteeg, W. Malasekera, Turbulence and its Modelling [M], second ed., Pearson Education Ltd, England, 2007, pp. 40–114.

[30] M. Han, Y. Liu, D. Wu, X. Zhao, H. Tan, A numerical investigation in characteristics of flow force under cavitation state inside the water hydraulic poppet valves, Int. J. Heat Mass Tran. 111 (2017) 1–16.

[31] B.K. Saha, Y. Wu, S. Li, Deflector optimization in reducing cavitation intensity in the pilot stage of deflector jet servo-valve, in: Proceedings of the 8th International Conference on Fluid Power and Mechatronics, FPM 2019, Institute of Electrical and Electronics Engineers Inc., Apr. 2019, pp. 1500–1507, https://doi.org/10.1109/FPM45753.2019.9035892.

[32] Z. Chen, S. Ge, Y. Jiang, W. Lin, Y. Zhu, Mathematical modeling of pressure characteristics of the deflector-jet pilot stage considering boundary layer flow, Flow Meas. Instrum. 90 (Apr. 2023) 102312, https://doi.org/10.1016/j.flowmeasinst.2023.102312.

[33] Y. Chu, Z. Yuan, X. He, Z. Dong, Model Construction and Performance Degradation Characteristics of a Deflector Jet Pressure Servo Valve under the Condition of Oil Contamination, International Journal of Aerospace Engineering 2021 (Feb. 2021) 1–17, https://doi.org/10.1155/2021/8840084.